Hybrid polar state in epitaxial (111) $PbSc_{0.5}Nb_{0.5}O_3$ relaxor ferroelectric films

J. Peräntie,[1,*] M. Savinov,[2] T. Kocourek,[2] M. Jelínek,[2] H. Jantunen,[1] A. Dejneka,[2] and M. Tyunina[1,2,†]
[1]*Microelectronics Research Unit, University of Oulu, P.O. Box 4500, FI-90014 Oulu, Finland*
[2]*Institute of Physics of the Czech Academy of Sciences, Na Slovance 2, 18221 Prague, Czech Republic*

(Received 29 August 2018; revised manuscript received 24 November 2018; published 10 January 2019)

In relaxor ferroelectrics, the interplay between the short-range-order dipolar state and long-range-order ferroelectric state leads to outstanding response functions, which enable valuable capacitor, electromechanical, pyroelectric, and electrocaloric applications. Advanced applications are envisaged with epitaxial relaxor ferroelectric films, whose fundamentals are still poorly explored. In particular, frustration of ferroelectricity, contrasting the bulk behavior, has been found and ascribed to nonpolar crystal orientation in (001) epitaxial films of archetypical lead-based relaxors. Here, a peculiar hybrid polar state, where coexisting long-range and short-range orders persist to very low temperatures, is demonstrated in epitaxial polar-oriented (111) $PbSc_{0.5}Nb_{0.5}O_3$ films. The hybrid state is evidenced by relaxorlike frustrations of ferroelectric transition and the Curie-Weiss behavior, validity of the Vogel-Fulcher relationship, a non-Rayleigh dynamic nonlinearity, and a ferroelectriclike low-temperature polarization. Local fluctuations of lattice strain arising from the relaxation of large epitaxial misfit are suggested to be responsible for the hybrid polar state. Introducing strain fluctuations by doping or nanostructuring is anticipated to boost the dynamic dielectric and piezoelectric performance of many perovskite oxide ferroelectrics.

DOI: 10.1103/PhysRevMaterials.3.014403

I. INTRODUCTION

Great advances in thin-film technology and research over the past three decades have resulted in the synthesis of epitaxial ferroelectric (FE) heterostructures with novel and enhanced properties [1–4]. Phase diagrams and polarization of epitaxially strained perovskite oxide FE films were theoretically predicted by phenomenological and *ab initio* calculations and the films exhibiting remarkable strain-induced behavior were experimentally demonstrated [5–14]. Contrasting the progress in studies of epitaxial FE films, similar development is still elusive with epitaxial perovskite relaxor ferroelectric (RFE) thin films.

Unlike the abrupt transition between the high-temperature nonpolar paraelectric (PE) state and the low-temperature long-range-ordered polar FE state in normal FEs, a short-range polar order and giant dipoles are present in the high-temperature relaxor (R) state in RFEs [15–18]. On cooling, RFEs undergo a spontaneous or an electric-field-induced phase transition from such R phase to a low-temperature FE phase [17]. The complex interplay between a short-range dipolar R state and long-range FE state leads to outstanding and unmatched response functions, which enable capacitor, electromechanical, pyroelectric, and electrocaloric applications of RFEs [19–24]. Advances in nanoscale applications are envisaged with epitaxial RFE films, and some of them have already been demonstrated [25,26]. Concurrently, the understanding of RFE behavior in epitaxial thin films continues to be a major challenge despite intensive theoretical efforts made in recent years [27–33]. In particular, understanding of the low-temperature state is crucial for achieving desired functionalities in epitaxial RFE films.

As found experimentally, bulk-type RFE behavior is not encountered with epitaxial (001) RFE films, where the dipolar R state is more stable. For instance, the temperature- and/or electric-field-induced R-to-FE phase transitions are frustrated in epitaxial (001) films of archetypical $PbMg_{1/3}Nb_{2/3}O_3$ (PMN) and $PbSc_{1/2}Nb_{1/2}O_3$ (PSN) RFEs [34–36]. The low-temperature polar phase differs from the bulk one and is not fundamentally ferroelectric in these films. Moreover, the R phase is robust in both epitaxially strained and nearly unstrained (001) RFE films. This observation suggests that the suppression of the FE transition may be more universally related to film-substrate coupling, especially substrate-induced (001) orientation of the films [34–37]. We note that in these films, the electric field is applied and responses are measured along the out-of-plane [001] direction, which contrasts with the [111] polar direction in PMN and PSN [18,38–41]. Thus, the out-of-plane (111) film orientation may favor bulklike RFE behavior with the low-temperature FE long-range-ordered state. However, in contrast to this expectation, we experimentally demonstrate here a hybrid polar state in epitaxial (111) PSN films, which exhibit frustrated FE transition and low-temperature coexistence of FE-like switching with R-like dipolar nonlinearity. Our observations evidence that the long-range and short-range polar orders concurrently persist to very low temperatures in these films. We discuss local fluctuations of lattice strain as responsible for the hybrid state in the films of PSN and other related materials.

*jani.perantie@oulu.fi
†marina.tjunina@oulu.fi

 ©2019 American Physical Society

II. EXPERIMENT

Epitaxial heterostructures of the PSN films using $SrRuO_3$ (SRO) bottom electrodes were grown by pulsed laser deposition (PLD) on (111) $SrTiO_3$ (STO) and (0001) Al_2O_3 (c-Al_2O_3) single-crystal substrates. Film thicknesses in the (111)PSN/SRO stacks were 300/20 nm on STO and 150/20 nm on Al_2O_3, while the increased (110) fraction was obtained in thicker PSN films on (0001)Al_2O_3. Reference heterostructures using films of normal FE tetragonal $PbZr_{0.2}Ti_{0.8}O_3$ and rhombohedral $PbZr_{0.65}Ti_{0.35}O_3$ were deposited on (001) $SrTiO_3$ and (0001) Al_2O_3 substrates for comparison. All films were grown at 700 °C and 20 Pa of ambient oxygen pressure.

The room-temperature crystal phases, orientation, epitaxy, and strain were analyzed using x-ray diffraction (XRD) on a high-resolution x-ray diffractometer (Bruker D8 Discover and Rigaku SmartLab) with CuKα_1/CuKα radiation. In-plane epitaxy and stacking were inspected by reciprocal space mapping and phi scans. Film lattice parameters were determined from the positions of diffraction peaks using substrates as a reference. Surface morphology of the films was studied by atomic force microscope (AFM, MultiMode 8, Bruker).

The dielectric and ferroelectric responses of the heterostructures were measured using a precision *LCR* meter (4284A, Agilent Technologies), an impedance analyzer (Alpha-AN, Novocontrol Technologies), and a ferroelectric test system (TF 2000 E Analyzer, aixACCT Systems GmbH). The electric field was applied and the responses were measured along the out-of-plane polar (111) direction of the PSN films. For the electrical characterization, SRO/PSN/Pt capacitors were formed by shadow-mask PLD of Pt top electrode pads. The capacitance and dielectric loss were determined as a function of frequency ($f = 10^2$–10^6 Hz), temperature ($T =$ 100–600 K), amplitude of ac voltage ($V_{AC} = 0.001$–3 V), and dc bias ($V_{DC} = 0$–10 V). The dynamic/quasistatic polarization and current loops were recorded as a function of applied voltage at $T = 100$–300 K and $f = 1$ kHz. Temperature control during the measurements was realized by a multiprobe thermal stage (THMS 600, Linkam Scientific Instruments) and flow cryostat (ST-100, Janis Research Company, LLC) equipped with temperature controller (Model 335, Lake Shore Cryotronics, Inc.).

III. RESULTS AND DISCUSSION

A. Crystal structure

Chemically disordered bulk PSN possesses a rhombohedral structure with lattice constant of $a_0 = 4.0828$ Å and $\alpha = 89.915°$ at room temperature [39]. Considering coherent epitaxial growth of (111) oriented pseudocubic perovskite cells of PSN and SRO on top of (111) STO and (0001) Al_2O_3 substrates [see, e.g., Refs. [42–47], the theoretical film-substrate misfit is large. In particular, the PSN-STO misfit is approximately $s = 1 - d_{1\bar{1}0}(\mathrm{PSN})/d_{1\bar{1}0}(\mathrm{STO}) = 1 - d_{11\bar{2}}(\mathrm{PSN})/d_{11\bar{2}}(\mathrm{STO}) \approx -4.6\%$ along the in-plane $[1\bar{1}0]$ and $[11\bar{2}]$ directions, correspondingly. Epitaxial (111) perovskite oxides (and face-centered-cubic metals) show two possible in-plane orientations on (0001) Al_2O_3 with $[1\bar{1}0]$ film direction aligned with substrate $[10\bar{1}0]$ or $[11\bar{2}0]$ directions [44,48,49].

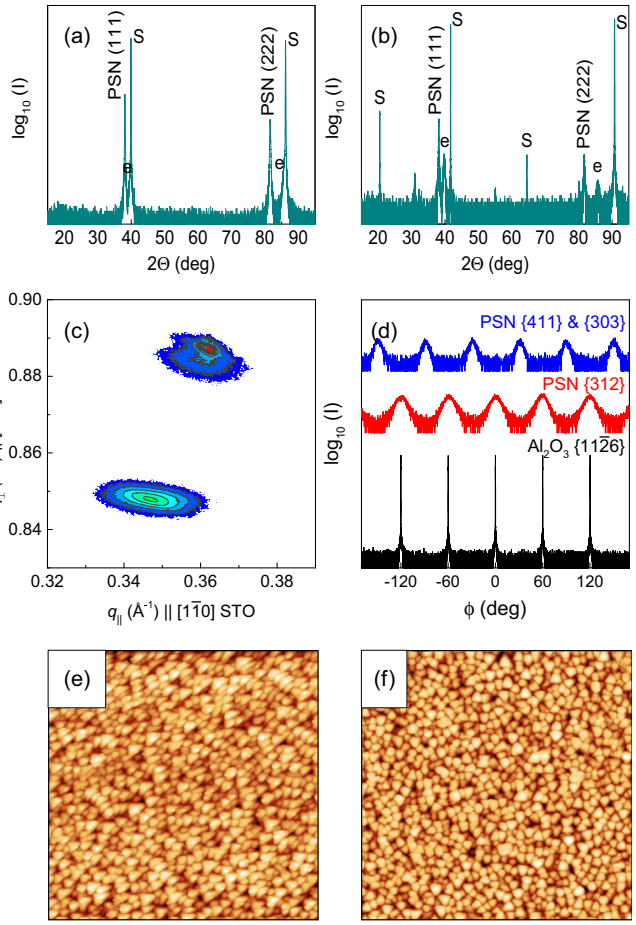

FIG. 1. (a),(b) XRD Θ-2Θ patterns in (a) PSN/SRO/STO and (b) PSN/SRO/c-Al_2O_3 with diffraction peaks from PSN, STO, and c-Al_2O_3 (substrate diffractions marked with S), and SRO bottom electrode (marked with "e"). (c) XRD reciprocal space map around the (312) lattice point in PSN/SRO/STO. (d) XRD phi scans through PSN (312), (303), (411) and Al_2O_3 ($11\bar{2}6$) reciprocal lattice points in PSN/SRO/c-Al_2O_3. (e),(f) AFM images of surface topography in (e) PSN/SRO/STO and (f) PSN/SRO/c-Al_2O_3. Scan size is 2×2 μm.

To estimate PSN-Al_2O_3 misfit, domain matching epitaxy is assumed [44,49–51]. (111) PSN shows the closest in-plane match along the close-packed Al_2O_3 $[10\bar{1}0]$ direction with mismatch of $s = 1 - d_{2\bar{2}0}(\mathrm{PSN})/d_{30\bar{3}0}(\mathrm{Al_2O_3}) \approx -5\%$. Other in-plane directions show higher lattice mismatches on c-plane Al_2O_3 and domain matching epitaxy is required. Similarly, the misfits are estimated for pseudocubic perovskite (111) SRO: -0.8% on STO and -1.2% on Al_2O_3. By extrapolating lattice parameters to the high deposition temperature, the misfits of -4.0% for PSN/STO and -4.9% for PSN/Al_2O_3 are estimated for film growth. For coherent growth of (111) SRO on (111) STO and (0001) Al_2O_3, the theoretical PSN-SRO misfits are close to the large PSN-substrate misfits. Despite these large misfits, highly oriented (111) PSN films possessing clear in-plane film-substrate epitaxial relationships are obtained here.

As evidenced by XRD Θ-2Θ scans, the (111) planes of perovskite cells of PSN and SRO are parallel to the (111) planes of STO [Fig. 1(a)] and (0001) planes of c-Al_2O_3 [Fig. 1(b)]. Neither the pyrochlore phase nor chemical ordering along the

(111) direction are detected in the PSN films. The presence of a small (110)-oriented PSN fraction is found in the stack on c-Al_2O_3 [Fig. 1(b), diffraction peak at ~31°]. From the (222) PSN peaks, the out-of-plane lattice spacing $d_{222} \approx 1.178(8)$ Å and $d_{222} \approx 1.178(4)$ Å is found for PSN on (111) STO and c-Al_2O_3, respectively. These values translate to pseudocubic unit-cell parameters of 4.083 Å and 4.082 Å, correspondingly.

The in-plane orientation and epitaxy of (111) PSN was deduced from an XRD reciprocal spaced map and/or phi scans (Figs. 1(c) and 1(d), Supplemental Material Fig. S2 [47]). The reciprocal space map around the (312) lattice point in the PSN/SRO/(111)STO stack confirmed the epitaxial relationship [Fig. 1(c)], and the extracted in-plane lattice spacing of $d_{1\bar{1}0} = 2.886(2)$ Å is consistent with the out-of-plane Θ-2Θ measurements. The phi scans of (111) PSN on c-Al_2O_3 show off-axis diffractions peaks from PSN {312} crystal planes at 60° intervals aligned with the substrate {11$\bar{2}$6} diffractions [Fig. 1(d)]. Other off-axis diffractions from {303}/{411} PSN planes were observed with 30° rotation in relation to the substrate in-plane [11$\bar{2}$0] direction. Additionally, phi scans of the {220} PSN diffractions show three- and sixfold symmetry for PSN/SRO/(111)STO and PSN/SRO/c-Al_2O_3 heterostructures, respectively [47]. This indicates that (111) PSN on c-Al_2O_3 has two crystal variants with epitaxial relationships of PSN[1$\bar{1}$0] (111)||Al_2O_3[11$\bar{2}$0](0001) and PSN[$\bar{1}$10] (111)||Al_2O_3[11$\bar{2}$0] (0001). Similar twin-related A- and B-type crystal variants with different out-of-plane stacking orders have been observed in other (111)-oriented films [48,52–54]. The (111) PSN on STO shows one type of crystal variant and the epitaxial relationship is PSN[1$\bar{1}$0](111)||STO[1$\bar{1}$0](111).

The deposited perovskite (111) PSN films possess lattice parameters which are close to the bulk parameter. This proximity implies efficient relaxation of epitaxial misfit strain in PSN. Such relaxation of large misfit strain is known to proceed through the formation of a nanocolumnar microstructure during Stranski-Krastanov epitaxial growth [55]. The resulting low-angle columnar boundaries do not destroy epitaxial relationships [55–59]. Consistent with the previous observations, epitaxial nanocolumns with lateral dimensions of 50–70 nm are also found in the PSN films [Figs. 1(e) and 1(f)].

We note that relaxation of large epitaxial strain also produces substantial inhomogeneities of lattice strain, which are indicated here by broad XRD peaks. Moreover, in contrast to monotonic strain distribution across film thickness [60], such inhomogeneities are random fluctuations of lattice strain on a nanometer-length scale [61,62]. Notably, these fluctuations do not have to be directly connected with misfit dislocations, but they can be produced by nonuniform stress fields resulting from dislocations and other structural defects [62]. The local random strain fluctuations were shown to be responsible for the unusual dynamic properties of FE $BaTiO_3$ films in strongly mismatched heterostructures [63]. Here, strain fluctuations lead to a hybrid polar state, revealed by the electrical characterization as described next.

B. Phase transition

In bulk PSN, a spontaneous R-FE phase transition occurs on cooling within the temperature region of $T_{FE} \approx 341$–384 K

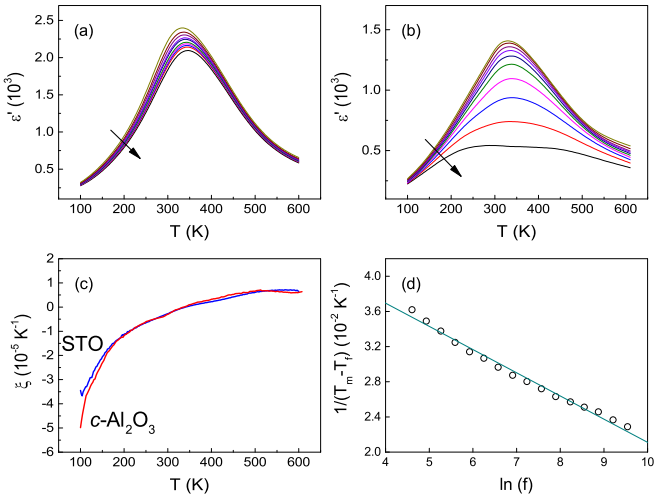

FIG. 2. (a),(b) The real part ε' of the relative dielectric permittivity at $f = 0.3$–12 kHz and (c) derivative of the inverse ξ of the relative dielectric permittivity at 2.2 kHz as a function of temperature on cooling for (a),(c) PSN/SRO/(111)STO and (b),(c) PSN/SRO/c-Al_2O_3 heterostructures. (d) The Vogel-Fulcher relationship fitting between the observed temperature of the maximum real part of dielectric permittivity T_m and the measurement frequency f (100 Hz–14 kHz) for the PSN/SRO/(111)STO thin-film heterostructure. Arrows in (a) and (b) show the direction of increasing frequency.

and it is manifested by an abrupt drop in the dielectric permittivity at temperatures below the temperature of the maximum permittivity $T_m > T_{FE}$ [18,34,38,64–68]. The frequency dispersion of T_m obeys the Vogel-Fulcher law in PSN, that is typical for the R state [18,68]. In thin-film capacitor heterostructures, tracking the R-FE or PE-FE transitions from the dielectric peaks is obscure because of extrinsic capacitor contributions to the measured dielectric response [35,69,70]. Also here, relatively high resistance of the bottom SRO electrode significantly contributes to frequency dispersion of the real part of the permittivity (ε') and loss tangent (tan δ) [47]. The effect makes it difficult to conclude on the FE or R state from the broad frequency-dependent dielectric peaks at around $T_m = 335$–350 K [Figs. 2(a) and 2(b)]. However, analysis of $T_m(f)$ at low frequencies is possible in PSN/SRO/STO. The analysis reveals the Vogel-Fulcher relationship with the fitted activation energy $E_a = 379$ K, freezing temperature $T_f = 300$ K, and averaged relaxation frequency $f_0 = 0.65 \times 10^8$ Hz [Fig. 2(d)]. The obtained frequency f_0 is small compared to typical frequencies of 10^{11}–10^{13} Hz in canonical bulk relaxors [18] and points to slowly relaxing polar entities: the corresponding average relaxation time is $\sim 1.5 \times 10^{-8}$ s.

A possible FE phase transition was investigated by plotting the derivative of inverse permittivity ξ as a function of temperature [Fig. 2(c)]. As shown before, the spontaneous onset of the FE state is evidenced by a constant value of $\xi(T)$, corresponding to the low-temperature Curie-Weiss behavior in PSN ceramics [34]. The shape of the $\xi(T)$ curves in the (111) PSN films does not indicate any FE state at low temperatures. The derivative $\xi(T)$ decreases gradually on cooling down to $T =$ 100 K without a low-temperature plateau or any detectable

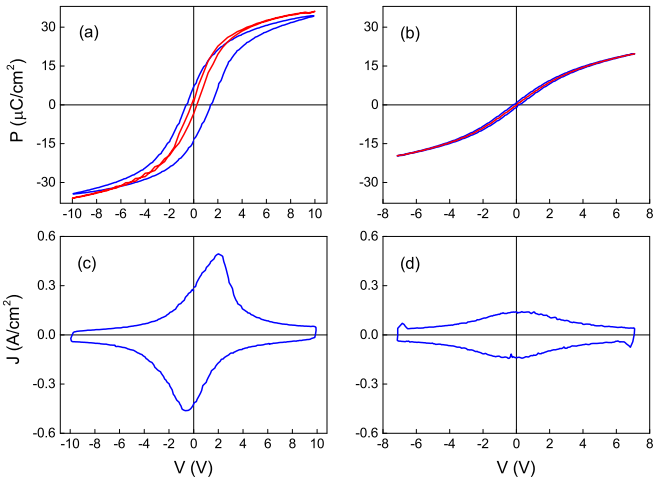

FIG. 3. (a),(b) Dynamic polarization (blue), quasistatic polarization (red), and (c),(d) dynamic current loops of relaxor ferroelectric (111) PSN thin films at $T = 300$ K and $f = 1$ kHz for (a),(c) PSN/SRO/(111)STO and (b),(d) PSN/SRO/c-Al_2O_3 thin-film heterostructures.

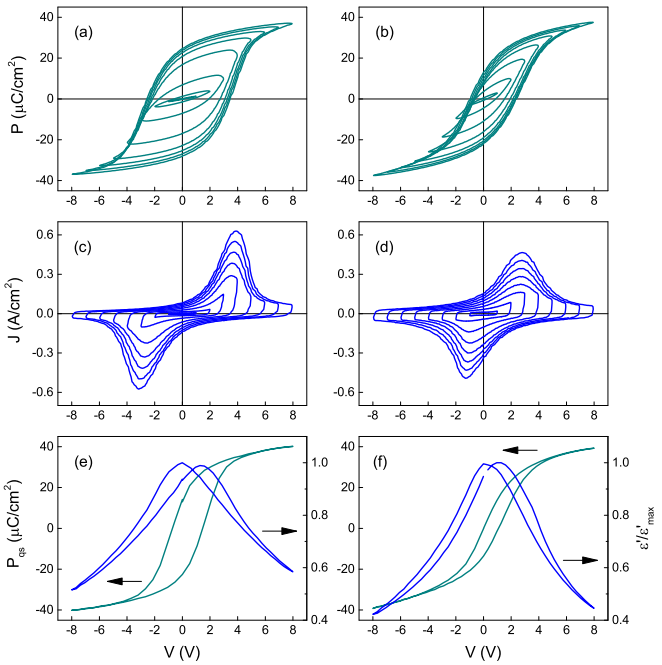

FIG. 4. (111) PSN polarization switching at $T = 100$ K: (a),(b) dynamic polarization P; (c),(d) dynamic switching current density J; and (e),(f) quasistatic polarization P_{qs} and normalized real part of relative permittivity $\varepsilon'/\varepsilon'_{max}$ as a function of applied voltage at $f = 1$ kHz. Results in (a),(c),(e) and (b),(d),(f) are measured for PSN/SRO/(111)STO and PSN/SRO/c-Al_2O_3 heterostructures, respectively.

deviation point to signify the onset of the phase transition. The shape of $\xi(T)$ at high temperatures (>500 K) is assigned to increased conduction of the PSN film. The observed $\xi(T)$ behavior is similar to that in epitaxial (001) RFE films and PMN crystal, and clearly differs from the behavior of PSN bulk and normal FE films [34,35,71,72].

The validity of the Vogel-Fulcher relationship and the low-temperature R-type derivative $\xi(T)$ show that the FE transition is frustrated in the (111) PSN films. This frustration contrasts the spontaneous FE transition, which is present in bulk PSN irrespective of different degrees of chemical order, doping, and defect concentrations, or grain size in ceramics [38,39,64,65,73]. On the other hand, a R-to-FE phase transition was not observed by dielectric measurements in fine-grained PSN ceramics (grain size $\leqslant$80 nm) [74]. The low-temperature non-FE state in the (111) PSN films is further explored by polarization measurements.

C. Polarization

The dielectric response suggests the low-temperature R state in the (111) PSN films. However, although the spontaneous FE transition is frustrated, an electric-field-induced FE transition is still possible in the R state. Thus, the PSN films are expected to show FE-type behavior below T_m under the application of external electric field along the [111] direction. To explore this possibility, ferroelectric properties, including polarization and switching, of the PSN films were tested by measuring dynamic polarization-voltage (P-V) and current-voltage (J-V) loops, quasistatic polarization-voltage (P_{qs}-V) loops where polarization is determined at each voltage point after a constant relaxation time of 1 s, and capacitance-voltage (C-V) characteristics in a temperature range of $T = 100$–300 K, below T_m.

Figure 3 presents the measured room-temperature dynamic and quasistatic loops for the studied (111) PSN films. Polarization loops are slim with small remanent polarization and coercive voltage values, especially for quasistatic loops. The measured minor dielectric hysteresis (C-V loops) is consistent with polarization loops [47]. The film behavior opposes a well-defined room-temperature polarization switching of the bulk PSN [67,68,75]. We note that extrinsic factors (e.g., high-resistance electrodes, small film thickness, clamping, etc.) may, in principle, lead to slim polarization loops in thin FE films [70,76,77]. However, such slim loops are not detected in our reference capacitors using films of normal FE $PbZr_{0.2}Ti_{0.8}O_3$ and $PbZr_{0.65}Ti_{0.35}O_3$ grown on SRO-coated STO and Al_2O_3 [47]. The reference $Pb(Zr,Ti)O_3$ films demonstrate well-defined hysteresis loops typical for a single-crystalline or ceramic bulk FEs. The obvious difference in the hysteresis behavior between the reference FE films and the (111) PSN films discards extrinsic factors as causing slim loops.

The polarization behavior evolves from the R-like to FE-like on cooling. The remanent polarization P_r and coercive field E_c increase monotonically on cooling and reach $P_r >$ 15–20 μC/cm^2 and $E_c \sim 100$ kV/cm at $T = 100$ K (Fig. 4). In addition to the FE-like P-V loops, the switching currents and butterfly-type C-V curves [Figs. 4(c)–4(f)] are also of FE character. The loops offset is caused by different electrode materials in the capacitors and by electric-field-induced dynamics in the films [36]. We stress that the FE-type switching behavior is evidenced only at the temperatures much lower than T_m in the (111) PSN films, which resembles behavior in epitaxial (001) PSN films [35]. Concurrently with the FE-like shape of the loops (Fig. 4), the remanent polarization

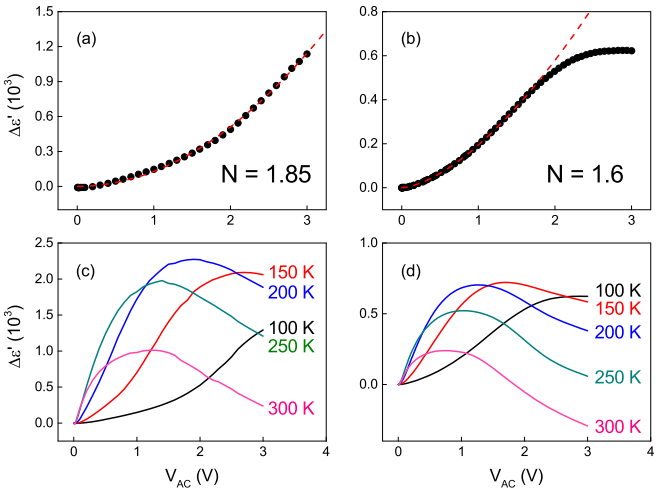

FIG. 5. The real part of dielectric permittivity change $\Delta\varepsilon'$ as a function of applied ac voltage amplitude V_{AC} and temperature at $f = 1$ kHz for (a),(c) PSN/SRO/(111)STO and (b),(d) PSN/SRO/c-Al_2O_3 thin-film heterostructures. Dotted lines in (a),(b) show the $\Delta\varepsilon' = \alpha {V_{AC}}^N$ fits at $T = 100$ K.

and saturation polarization increase with maximum applied voltage (Supplemental Material, Fig. S7 [47]). Such increase is consistent with the electric-field-induced dipolar flips and flow of a field-induced R-FE phase boundary [36].

D. Dipolar dynamics

To get better insight into the polar state in the (111) PSN films, we study dynamic dielectric responses as a function of ac drive therein. In normal FE materials, the subswitching domain-wall motion produces the Rayleigh-type linear dependence of permittivity on amplitude E_{AC} of the ac field, i.e., $\varepsilon'(E_{AC}) = \varepsilon'(0) + \alpha E_{AC}$ [78]. In the absence of FE domains and domain walls, the dielectric response of RFEs is determined by thermally and/or electrically activated flips of giant dipoles, and the behavior of $\varepsilon'(E_{AC})$ is more complex [17,79]. For instance, in relaxor PMN crystal, the nonlinear permittivity $\Delta\varepsilon'$ obeys a quadratic ac field dependence [i.e., $\Delta\varepsilon' = \varepsilon'(E_{AC}) - \varepsilon'(0) \propto {E_{AC}}^2$] at small fields and power dependence at higher fields [80,81]. Experimentally, quadratic dependence of $\Delta\varepsilon'$ on E_{AC} was found at low fields for (001) RFE epitaxial thin films of PMN, PMN-$PbTiO_3$, and PSN [69,82].

The measured $\Delta\varepsilon'$ versus V_{AC} dependencies for PSN/SRO/(111)STO and PSN/SRO/c-Al_2O_3 heterostructures are presented in Fig. 5 up to $V_{AC} = 3$ V (corresponds to E_{AC} of 100 and 200 kV/cm). The nonlinear permittivity $\Delta\varepsilon'$ at $T = 100$ K was fitted with the power function up to $E_{AC} = 100$ kV/cm, and exponent values of $N = 1.85$ and $N = 1.6$ were extracted for PSN/SRO/(111)STO and PSN/SRO/c-Al_2O_3 thin-film heterostructures, respectively (Figs. 5(a) and 5(b), Supplemental Material Fig. S8 [47]). The E_{AC} range used in fitting extends approximately to the coercive fields' values found in the polarization measurements [Figs. 4(a) and 4(b)]. The obtained exponents evidence the dipolar dynamics, different from the Rayleigh-type FE domain-wall motion. Thus, giant dipoles rather than normal FE domains are present in the (111) PSN films at low T. Also, at higher temperatures of 150–300 K, the dynamics is of dipolar character. The field dependence of the nonlinear part of the PSN permittivity shows a maximum, which shifts to lower ac voltages with increasing temperature [Figs. 5(c) and 5(d)]. This behavior is consistent with the theoretical simulations of dipolar dynamics and previous observations in epitaxial PMN films [32,82,83]. The results in Fig. 5 imply the presence of dipoles in the low-temperature state (below T_m) of the (111) PSN films.

E. Discussion

Our experimental studies of the (111) PSN films revealed that in contrast to bulk behavior, spontaneous R-FE transition is frustrated, giant dipoles remain present on cooling below T_m, and dipolar relaxation is very slow around T_m in the films. Concurrently, the electric-field-induced low-temperature state is FE-like. The detected coexistence of the R-like and FE-like features implies a hybrid polar state, where the short-range polar order coexists with the long-range one. Because similar observations were done in the (001) epitaxial films of PSN and PMN, we discard the film orientation as responsible for the hybrid state.

We note that the coexistence of short- and long-range polar orders was recently detected in epitaxial films of normal FE $BaTiO_3$ (BTO) on STO [63]. Concurrently, relaxation of large epitaxial misfit was found to result in significant random fluctuations of lattice strain in such BTO films [61,62]. Because of strain-polarization coupling in BTO, strain fluctuations produce fluctuations of polarization, leading to polar nanoregions or giant dipoles. The strain-fluctuation-induced giant dipoles (or strain dipoles here for brevity) interact elastically and electrically compared to mainly electrical interaction between dipoles, related to cationic B^I–B^{II} charge imbalance in $Pb(B^I,B^{II})O_3$ RFEs. Due to their elastic origin and interactions, the strain dipoles possess longer relaxation times than RFE dipoles. Similar to RFE dipoles, the strain dipoles manifest themselves in such R-like features as Vogel-Fulcher behavior, deviation from the Curie-Weiss law, and non-Rayleigh dynamic nonlinearity.

The strain dipoles can originate from the relaxation of large epitaxial misfit in the (111) PSN films and in the previously reported (001) PSN and PMN films. The relaxation time of $\sim 10^{-8}$ s is significantly longer than for RFE dipoles that confirms the presence of the strain dipoles here. The strain dipoles are responsible for the observed R-type features, pertaining to the very low temperatures.

We stress that fluctuations of lattice strain can lead to giant dipoles only in such materials, where polarization is a strong enough function of strain. For instance, this is not the case in $PbTiO_3$ and $Pb(Zr,Ti)O_3$ [7,9]. Therefore, relaxation of large misfit and related fluctuations of lattice strain have no detectable impact on normal FE behavior in thin films of these perovskites. The FE properties of our reference $Pb(Zr,Ti)O_3$ films comply with this trend [47].

Finally, we note that the strain dipoles and hybrid polar state are naturally formed here through misfit relaxation. However, strain fluctuations can also be created by appropriate doping or nanostructuring, allowing for a hybrid polar

state not only in thin films, but also in bulk samples and thick layers. We anticipate that advanced dynamic dielectric and piezoelectric performance can be achieved by introducing strain fluctuations in many perovskite oxide FEs.

IV. CONCLUSIONS

Heterostructures of perovskite (111) PSN films and (111) SRO bottom electrodes are grown on (111) $SrTiO_3$ and (0001) Al_2O_3 substrates. Epitaxy and relaxation of large misfit strain are revealed in the PSN films. The dielectric response and polarization are inspected as a function of temperature, frequency, amplitude of ac voltage, and dc bias in the Pt/PSN/SRO stacks. The relaxorlike frustration of the ferroelectric transition, the Vogel-Fulcher relationship, deviation from the Curie-Weiss behavior, and non-Rayleigh dynamic nonlinearity are found to coexist with the ferroelectriclike low-temperature polarization in PSN, implying a hybrid polar state, where the short-range polar order coexists with the long-range one. The hybrid polar state is caused by local strain fluctuations, which arise from misfit relaxation and produce polarization fluctuations owing to strain-polarization coupling. Enhanced dynamic dielectric and piezoelectric properties are expected for a hybrid polar state in many other perovskite oxide ferroelectrics, where strain fluctuations are induced by doping or nanostructuring.

ACKNOWLEDGMENTS

The work was supported by the Academy of Finland (Grant No. 298409) and in part by the European Structural and Investment Funds and Ministry of Education, Youth and Sports of the Czech Republic through Programme "Research, Development and Education" (Project No. SOLID21 - CZ.02.1.01/0.0/0.0/16_019/0000760).

[1] C. H. Ahn, K. M. Rabe, and J.-M. Triscone, Science **303**, 488 (2004).
[2] N. Setter, D. Damjanovic, L. Eng, G. Fox, S. Gevorgian, S. Hong, A. Kingon, H. Kohlstedt, N. Y. Park, G. B. Stephenson, I. Stolitchnov, A. K. Tagantsev, D. V. Taylor, T. Yamada, and S. Streiffer, J. Appl. Phys. **100**, 051606 (2006).
[3] D. G. Schlom, L.-Q. Chen, C.-B. Eom, K. M. Rabe, S. K. Streiffer, and J.-M. Triscone, Annu. Rev. Mater. Res. **37**, 589 (2007).
[4] L. W. Martin, Y.-H. Chu, and R. Ramesh, Mater. Sci. Eng. R **68**, 89 (2010).
[5] N. A. Pertsev, A. G. Zembilgotov, and A. K. Tagantsev, Phys. Rev. Lett. **80**, 1988 (1998).
[6] V. G. Koukhar, N. A. Pertsev, and R. Waser, Phys. Rev. B **64**, 214103 (2001).
[7] C. Ederer and N. A. Spaldin, Phys. Rev. Lett. **95**, 257601 (2005).
[8] V. G. Kukhar, N. A. Pertsev, H. Kohlstedt, and R. Waser, Phys. Rev. B **73**, 214103 (2006).
[9] N. A. Pertsev and B. Dkhil, Appl. Phys. Lett. **93**, 122903 (2008).
[10] K. J. Choi, M. Biegalski, Y. L. Li, A. Sharan, J. Schubert, R. Uecker, P. Reiche, Y. B. Chen, X. Q. Pan, V. Gopalan, L.-Q. Chen, D. G. Schlom, and C. B. Eom, Science **306**, 1005 (2004).
[11] I. Vrejoiu, G. Le Rhun, L. Pintilie, D. Hesse, M. Alexe, and U. Gösele, Adv. Mater. **18**, 1657 (2006).
[12] J. Karthik, A. R. Damodaran, and L. W. Martin, Phys. Rev. Lett. **108**, 167601 (2012).
[13] J. Karthik, J. C. Agar, A. R. Damodaran, and L. W. Martin, Phys. Rev. Lett. **109**, 257602 (2012).
[14] L. Feigl, P. Yudin, I. Stolichnov, T. Sluka, K. Shapovalov, M. Mtebwa, C. S. Sandu, X.-K. Wei, A. K. Tagantsev, and N. Setter, Nat. Commun. **5**, 4677 (2014).
[15] L. E. Cross, Ferroelectrics **76**, 241 (1987).
[16] G. A. Samara, J. Phys.: Condens. Matter **15**, R367 (2003).
[17] A. A. Bokov and Z.-G. Ye, J. Mater. Sci. **41**, 31 (2006).
[18] Y.-H. Bing, A. A. Bokov, and Z.-G. Ye, Curr. Appl. Phys. **11**, S14 (2011).
[19] S.-E. Park and T. R. Shrout, J. Appl. Phys. **82**, 1804 (1997).
[20] Y. Tang, X. Wan, X. Zhao, X. Pan, D. Lin, and H. Luo, J. Appl. Phys. **98**, 084104 (2005).
[21] Z. Feng, X. Zhao, and H. Luo, J. Am. Ceram. Soc. **89**, 3437 (2006).
[22] B. Rožič, M. Kosec, H. Uršič, J. Holc, B. Malič, Q. M. Zhang, R. Blinc, R. Pirc, and Z. Kutnjak, J. Appl. Phys. **110**, 064118 (2011).
[23] F. Li, S. Zhang, T. Yang, Z. Xu, N. Zhang, G. Liu, J. Wang, J. Wang, Z. Cheng, Z.-G. Ye, J. Luo, T. R. Shrout, and L.-Q. Chen, Nat. Commun. **7**, 13807 (2016).
[24] F. Li, D. Lin, Z. Chen, Z. Cheng, J. Wang, C. Li, Z. Xu, Q. Huang, X. Liao, L.-Q. Chen, T. R. Shrout, and S. Zhang, Nat. Mater. **17**, 349 (2018).
[25] S. H. Baek, J. Park, D. M. Kim, V. A. Aksyuk, R. R. Das, S. D. Bu, D. A. Felker, J. Lettieri, V. Vaithyanathan, S. S. N. Bharadwaja, N. Bassiri-Gharb, Y. B. Chen, H. P. Sun, C. M. Folkman, H. W. Jang, D. J. Kreft, S. K. Streiffer, R. Ramesh, X. Q. Pan, S. Trolier-McKinstry, D. G. Schlom, M. S. Rzchowski, R. H. Blick, and C. B. Eom, Science **334**, 958 (2011).
[26] S. Pandya, J. Wilbur, J. Kim, R. Gao, A. Dasgupta, C. Dames, and L. W. Martin, Nat. Mater. **17**, 432 (2018).
[27] A. R. Akbarzadeh, S. Prosandeev, E. J. Walter, A. Al-Barakaty, and L. Bellaiche, Phys. Rev. Lett. **108**, 257601 (2012).
[28] A. Al-Barakaty, S. Prosandeev, D. Wang, B. Dkhil, and L. Bellaiche, Phys. Rev. B **91**, 214117 (2015).
[29] S. Prosandeev, D. Wang, A. R. Akbarzadeh, and L. Bellaiche, J. Phys.: Condens. Matter **27**, 223202 (2015).
[30] S. Prosandeev and L. Bellaiche, Phys. Rev. B **94**, 180102 (2016).
[31] Z. Jiang, S. Prokhorenko, S. Prosandeev, Y. Nahas, D. Wang, J. Íñiguez, E. Defay, and L. Bellaiche, Phys. Rev. B **96**, 014114 (2017).
[32] J. Liu, F. Li, Y. Zeng, Z. Jiang, L. Liu, D. Wang, Z.-G. Ye, and C.-L. Jia, Phys. Rev. B **96**, 054115 (2017).
[33] Y. Nahas, A. Akbarzadeh, S. Prokhorenko, S. Prosandeev, R. Walter, I. Kornev, J. Íñiguez, and L. Bellaiche, Nat. Commun. **8**, 15944 (2017).

[34] M. Tyunina, J. Levoska, P.-E. Janolin, and A. Dejneka, Phys. Rev. B **87**, 224107 (2013).

[35] M. Tyunina, I. Pintilie, A. Iuga, M. S. Stratulat, and L. Pintilie, J. Phys.: Condens. Matter **26**, 325901 (2014).

[36] M. Tyunina, I. Pintilie, A. Iuga, and L. Pintilie, Phys. Rev. B **89**, 094106 (2014).

[37] M. Tyunina, J. Levoska, D. Nuzhnyy, and S. Kamba, Phys. Rev. B **81**, 132105 (2010).

[38] C. Malibert, B. Dkhil, J. M. Kiat, D. Durand, J. F. Bérar, and A. Spasojevic-de Biré, J. Phys.: Condens. Matter **9**, 7485 (1997).

[39] C. Perrin, N. Menguy, E. Suard, Ch. Muller, C. Caranoni, and A. Stepanov, J. Phys.: Condens. Matter **12**, 7523 (2000).

[40] N. Takesue, Y. Fujii, and H. You, Phys. Rev. B **64**, 184112 (2001).

[41] I.-K. Jeong, T. W. Darling, J. K. Lee, Th. Proffen, R. H. Heffner, J. S. Park, K. S. Hong, W. Dmowski, and T. Egami, Phys. Rev. Lett. **94**, 147602 (2005).

[42] H. Funakubo, T. Oikawa, N. Higashi, and K. Saito, J. Cryst. Growth **235**, 401 (2002).

[43] W. Gong, J.-F. Li, X. Chu, Z. Gui, and L. Li, Appl. Phys. Lett. **85**, 3818 (2004).

[44] S. K. Dey, C. G. Wang, W. Cao, S. Bhaskar, J. Li, and G. Subramanyam, J. Mater. Sci. **41**, 77 (2006).

[45] H. Kuwabara, N. Menou, and H. Funakubo, Appl. Phys. Lett. **90**, 222901 (2006).

[46] D. Rubi, A. H. G. Vlooswijk, and B. Noheda, Thin Solid Films **517**, 1904 (2009).

[47] See Supplemental Material at http://link.aps.org/supplemental/10.1103/PhysRevMaterials.3.014403 for schematic description of substrate surfaces (Fig. S1), additional XRD phi scans (Fig. S2), complementary dielectric results as a function of temperature, frequency, and electric field (Figs. S3–S5, S7, and S8), and polarization hysteresis loops of reference PZT films (Fig. S6).

[48] S. Schmidt, J. Lu, S. P. Keane, L. D. Bregante, D. O. Klenov, and S. Stemmer, J. Am. Ceram. Soc. **88**, 789 (2005).

[49] K. Inaba, S. Kobayashi, K. Uehara, A. Okada, S. L. Reddy, and T. Endo, Adv. Mater. Phys. Chem. **03**, 72 (2013).

[50] T. Zheleva, K. Jagannadham, and J. Narayan, J. Appl. Phys. **75**, 860 (1994).

[51] J. Narayan and B. C. Larson, J. Appl. Phys. **93**, 278 (2003).

[52] F. Sánchez, R. Bachelet, P. de Coux, B. Warot-Fonrose, V. Skumryev, L. Tarnawska, P. Zaumseil, T. Schroeder, and J. Fontcuberta, Appl. Phys. Lett. **99**, 211910 (2011).

[53] G. Panomsuwan, O. Takai, and N. Saito, Solid State Commun. **158**, 65 (2013).

[54] G. Panomsuwan, O. Takai, and N. Saito, Appl. Phys. Lett. **103**, 112902 (2013).

[55] J. Q. He, E. Vasco, R. Dittmann, and R. H. Wang, Phys. Rev. B **73**, 125413 (2006).

[56] S. Y. Hou, J. Kwo, R. K. Watts, J.-Y. Cheng, and D. K. Fork, Appl. Phys. Lett. **67**, 1387 (1995).

[57] X. W. Wang, X. Wang, W. J. Gong, Y. Q. Zhang, Y. L. Zhu, Z. J. Wang, and Z. D. Zhang, Thin Solid Films **520**, 2785 (2012).

[58] M. Tyunina, L. Yao, M. Plekh, J. Levoska, and S. van Dijken, Adv. Funct. Mater. **23**, 467 (2013).

[59] L. Yao, S. Inkinen, O. Pacherova, M. Jelinek, S. van Dijken, and M. Tyunina, Phys. Chem. Chem. Phys. **20**, 4263 (2018).

[60] G. Catalan, B. Noheda, J. McAneney, L. J. Sinnamon, and J. M. Gregg, Phys. Rev. B **72**, 020102(R) (2005).

[61] M. Klinger, L. Polívka, A. Jäger, and M. Tyunina, J. Appl. Cryst. **49**, 762 (2016).

[62] V. Gartnerova, O. Pacherova, M. Klinger, M. Jelinek, A. Jagera, and M. Tyunina, Mater. Res. Bull. **89**, 180 (2017).

[63] M. Tyunina and M. Savinov, Phys. Rev. B **94**, 054109 (2016).

[64] F. Chu, I. M. Reaney, and N. Setter, J. Appl. Phys. **77**, 1671 (1995).

[65] C. Perrin, N. Menguy, O. Bidault, C. Y. Zahra, A.-M. Zahra, C. Caranoni, B. Hilczer, and A. Stepanov, J. Phys.: Condens. Matter **13**, 10231 (2001).

[66] E. L. Venturini, R. K. Grubbs, G. A. Samara, Y. Bing, and Z.-G. Ye, Phys. Rev. B **74**, 064108 (2006).

[67] Z. Wang and X. Long, Cryst. Eng. Comm. **16**, 6588 (2014).

[68] S. Huo, A. A. Bokov, A. Paterson, and Z.-G. Ye, Phase Trans. **88**, 1018 (2015).

[69] M. Tyunina, J. Levoska, and S. Leppävuori, J. Mater. Sci.-Mater. Electron. **14**, 369 (2003).

[70] M. Tyunina and J. Levoska, Appl. Phys. Lett. **88**, 262904 (2006).

[71] M. Tyunina, M. Plekh, and J. Levoska, Phys. Rev. B **79**, 054105 (2009).

[72] M. Tyunina, M. Plekh, M. Antonova, and A. Kalvane, Phys. Rev. B **84**, 224105 (2011).

[73] O. Bidault, C. Perrin, C. Caranoni, and N. Menguy, J. Appl. Phys. **90**, 4115 (2001).

[74] M. Ivanov, J. Banys, C. Bogicevic, and J.-M. Kiat, Ferroelectrics **429**, 43 (2012).

[75] H. Uršič, S. Drnovsek, and B. Malič, J. Phys. D: Appl. Phys. **49**, 115304 (2016).

[76] L. Pintilie, J. Optoelectron. Adv. Mater. **11**, 215 (2009).

[77] L. Jin, F. Li, and S. Zhang, J. Am. Ceram. Soc. **97**, 1 (2014).

[78] D. V. Taylor and D. Damjanovic, J. Appl. Phys. **82**, 1973 (1997).

[79] Z.-R. Liu, B.-L. Gu, and X.-W. Zhang, Phys. Rev. B **62**, 1 (2000).

[80] C. Filipič, A. Levstik, and Z. Kutnjak, Ferroelectrics **257**, 63 (2001).

[81] A. K. Tagantsev and A. E. Glazounov, Phase Trans. **65**, 117 (1998).

[82] M. Tyunina and J. Levoska, Phys. Rev. B **72**, 104112 (2005).

[83] M. Tyunina, J. Levoska, and I. Jaakola, Phys. Rev. B **74**, 104112 (2006).